Edge topology and flows in the reversed-field pinch

2012 Nucl. Fusion 52 054015

(http://iopscience.iop.org/0029-5515/52/5/054015)

IOP Publishing and International Atomic Energy Agency Nuclear Fusion
Nucl. Fusion **52** (2012) 054015 (11pp) doi:10.1088/0029-5515/52/5/054015

Edge topology and flows in the reversed-field pinch

G. Spizzo, M. Agostini, P. Scarin, N. Vianello, R. B. White[1], S. Cappello, M. E. Puiatti, M. Valisa and the RFX-mod Team

Consorzio RFX, Associazione Euratom-ENEA sulla fusione, C.so Stati Uniti 4, I-35127 Padova, Italy
[1] Plasma Physics Laboratory, Princeton University, PO Box 451, Princeton, NJ 08543, USA

E-mail: gianluca.spizzo@igi.cnr.it

Received 17 May 2011, accepted for publication 20 September 2011
Published 9 May 2012
Online at stacks.iop.org/NF/52/054015

Abstract
Edge topology and plasma flow deeply influence transport in the reversed-field pinch as well as in all fusion devices, playing an important role in many practical aspects of plasma performance, such as access to enhanced confinement regimes, the impact on global power balance and operative limits, such as the density limit (Spizzo G. *et al* 2010 *Plasma Phys. Control. Fusion* **52** 095011).

A central role is played by the edge electric field, which is determined by the ambipolar constraint guaranteeing quasi-neutrality in a sheath next to the plasma wall. Its radial component is experimentally determined in RFX over the whole toroidal angle by means of a diagnostic set measuring edge plasma potential and flow with different techniques (Scarin P. *et al* 2011 *Nucl. Fusion* **51** 073002). The measured radial electric field is used to construct the potential in the form $\Phi(\psi_p, \theta, \zeta)$ (ψ_p radial coordinate, θ, ζ angles), by means of the Hamiltonian guiding-centre code Orbit. Simulations show that a proper functional form of the potential can balance the differential radial diffusion of electrons and ions subject to $m = 0$ magnetic island O- and X-points. Electrons spend more time in the X-points of such islands than in O-points; ions have comparatively larger drifts and their radial motion is more uniform over the toroidal angle. The final spatial distribution of $\Phi(\psi_p, \theta, \zeta)$ results in a complex 3D pattern, with convective cells next to the wall. Generally speaking, an edge topology dominating parallel transport with a given symmetry brings about an edge potential with the same symmetry. This fact helps us to build a first step of a unified picture of the effect of magnetic topology on the Greenwald limit, and, more generally, on flows in the edge of RFPs and tokamaks.

(Some figures may appear in colour only in the online journal)

1. Introduction

Compelling evidence in the field of magnetically confined fusion devices shows that the edge magnetic topology influences plasma flow, and this in turn determines many practical aspects of plasma performance, such as access to enhanced confinement regimes, the impact on global power balance and operative limits, such as the density limit [1]. While studies of magnetic topology are mandatory in the reversed-field pinch (RFP), where enhanced confinement is by definition obtained through a bifurcation in the topology of magnetic field lines, from a chaotic regime [2] to a helical equilibrium [3–5] (see figure 1), such studies are more recent in the tokamak community, where the application of resonant magnetic perturbations (RMPs) in the edge is done purposely to stabilize the configuration with respect to the edge localized modes (ELMs) [6, 7] or the multifaceted asymmetric radiation from the edge (MARFE) [8, 9]. A common observation of RFPs and tokamaks is that the presence of a tangled magnetic topology in the edge influences the sign of the radial component of the edge electric field, E_r. In the tokamak, the application of the RMP changes the sign of E_r [10] and of the associated poloidal flow v_θ [11]: typically, the potential well present in the edge is reduced by the application of RMPs (more positive-outward E_r). In the RFP, the edge is naturally characterized by the presence of islands and weak chaos [12, 13], due to the reversal of the toroidal magnetic field B_ϕ in the edge, with the presence of a surface where $B_\phi = 0$ (reversal surface) and a small, negative B_ϕ at the wall, $B_\phi(a) \lesssim 0$. It is also observed that the electric field E_r (equivalently, toroidal velocity v_ϕ) changes sign along the toroidal angle ϕ, being a footprint of the underlying magnetic topology [14–16].

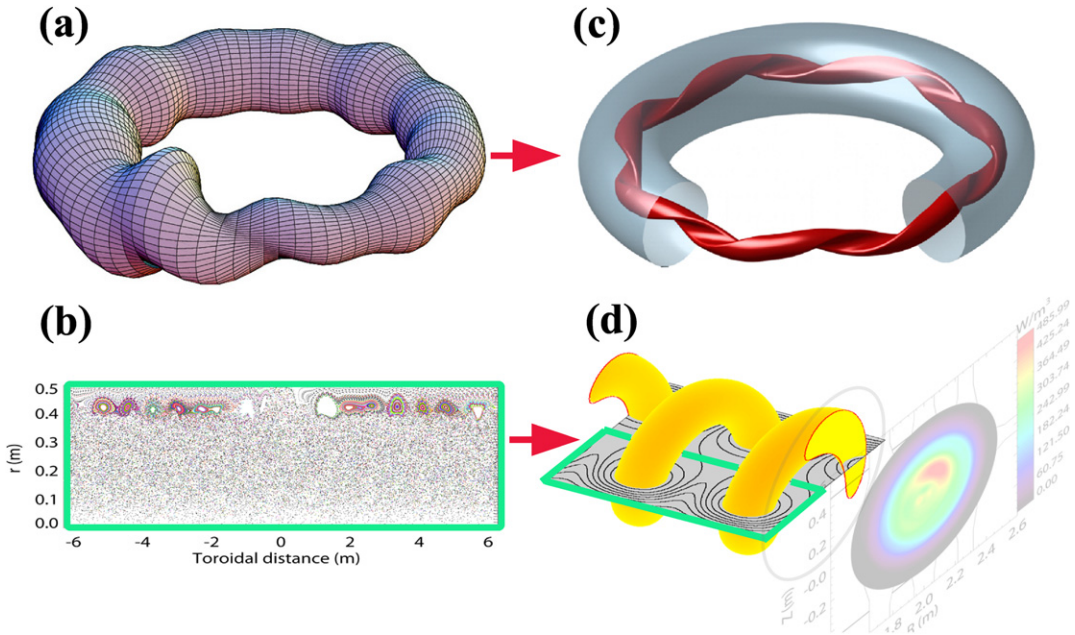

Figure 1. Artist's view of the bifurcation dominating RFP plasmas: (*a*), (*b*) the chaotic, multiple helicity—MH state, (*c*), (*d*) the helical equilibrium found in quasisingle helicity-QSH magnetic spectra. (*a*) and (*c*) are reconstructions of the plasma shape, 10× the real deformation in (*a*), showing that a plasma with a localized bulge in MH evolves towards a more uniform, helical shape in QSH. The inner magnetic topology is revealed in panels (*c*) and (*d*): in (*c*) it is evident that the MH state corresponds to chaos in the plasma core, with a residual chain of edge islands resonating at $q = 0$; panel (*d*) shows instead the well-conserved helical flux surfaces in the core, which correspond to increased emission in the soft-x-ray tomographic map.

Moreover, recent results show that the access to the helical state [17] and, generally speaking, the confinement and the behaviour of the configuration near operative limits, such as the Greenwald limit [16], are influenced by edge plasma, namely the modulation of E_r and the flow in the edge. Finally, studies of the edge topology in the RFP are favourable since the device is ohmic, circular and without divertor [18], in a way that it is easy to measure and to simulate.

In this paper we will propose a model explaining the modulation of the electric field in the edge: we will show that a tangled magnetic topology causes a differential radial diffusion of electrons and ions. The resulting electric fields (determined by the ambipolar constraint) can influence the flow and finally transport on a macroscopic scale, e.g. overall confinement and access to the helical state. In this work we will concentrate on the density limit, which in its extreme situation is a paradigm of edge transport, and is obtained mainly in the chaotic state of the RFP, where the edge geometry is essentially $m = 0$ (m poloidal mode number, i.e. the θ coordinate is ignorable for most purposes). The topology and associated transport is studied with the Hamiltonian guiding-centre code ORBIT [19]. Results are applicable to tokamak RMPs, where particle confinement and recycling have been measured to depend on the edge magnetic topology, namely on the spatial extent of the stochastic layer and the amount of field lines with short-connection length attached to the wall [20, 21]. The paper is organized as follows: in section 2 the background of the Greenwald limit in the RFP is briefly recalled; in section 3 test-particle simulations (without ambipolar potential) are presented; in section 4 the results with the potential are shown, and in section 5 we draw our conclusions and discuss open issues.

2. Background

The density limit (or 'Greenwald' limit) still defies a comprehensive theoretical explanation, even if in tokamaks and RFPs it can be characterized phenomenologically in terms of the Greenwald density [1], namely $n_G = I_p/\pi a^2$ (n_G in 10^{20} m^{-3}, I_p in MA). In the RFX-mod RFP device ($R_0 = 2$ m, $a = 45.9$ cm) [18] the phenomenology of the density limit has been already extensively described elsewhere [14–16, 22, 23]: here we provide a brief review of the subject. In the RFP, a central role in determining the Greenwald limit is played by the edge density: by increasing n_e/n_G (central density normalized to Greenwald) temperature decreases and density increases in the edge. The edge density accumulation takes place at $n_e \approx n_G$ in the chaotic, multiple helicity (MH) state, being preceded by a back-transition from the nice helical equilibrium (quasi-single helicity-QSH) to MH at $n_e/n_G \sim 0.4$ (see again figure 1 and [17]). The edge density accumulation causes an increase in the total radiation and O IV–O VI line emission, in the shape of a ring localized toroidally and poloidally symmetric ($m = 0$), in analogy with the MARFE [24] in tokamaks, which is a structure characterized by very low temperature and strong recombination, toroidally symmetric and poloidally localized ($n = 0$, n toroidal mode number). It is the MARFE in the tokamak, and its poloidal analogue in the RFP, which ultimately cause the discharge termination (often disruptive in the tokamak, never disruptive in the RFP [23]).

The huge edge density peak measured in the RFP at $n_e/n_G \sim 1$, which is the initial trigger of the whole density limiting phenomenon, cannot be sustained by local diffusion, $D\partial n_{edge}/\partial r$ [14]. A breakthrough for the explanation of this apparently odd phenomenon has been the analysis of the

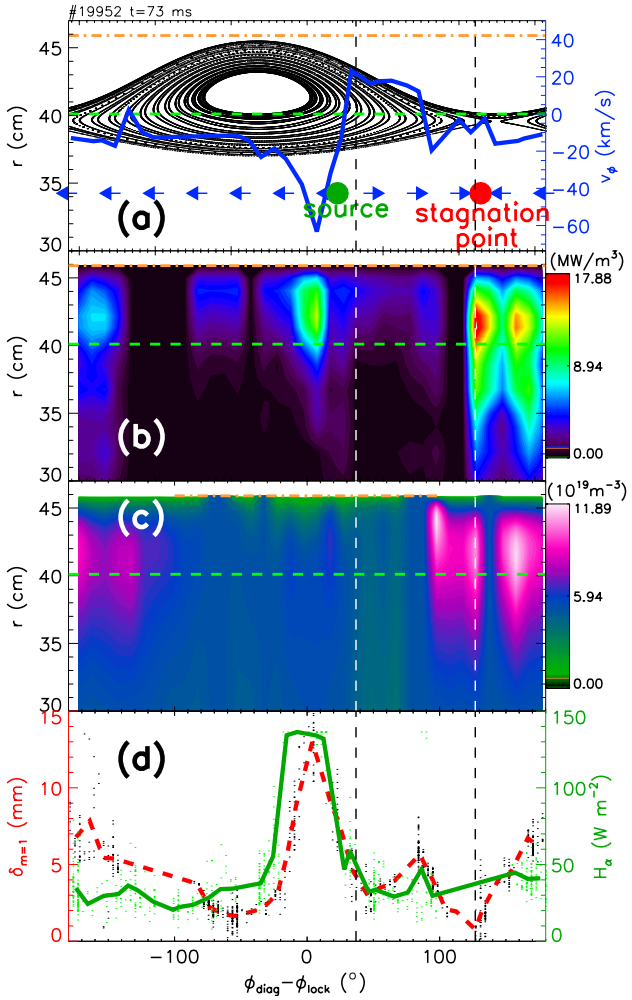

Figure 2. Toroidal patterns of total radiation and plasma flow: (*a*) plasma flow as a function of the normalized toroidal angle, $\phi - \phi_{\rm lock}$ (zero=maximum $m = 1$ bulge), for a discharge with $n_{\rm e}/n_{\rm G} = 0.8$. The Poincaré plot of the island associated with the $m = 0$,$n = 1$ mode is also shown; (*b*) for the same discharge, tomographic map of total radiation (minor radius as the *y*-axis); (*c*) map of electron density obtained from a multichord interferometer as a function of the toroidal angle; (*d*) H_α emissivity(solid) and $m = 1$ perturbation (dashed). The stagnation point for the plasma flow corresponds to the X-point of the island and to the maximum radiation and density, the other null point (=the source) corresponds to the peak of the influxes. The dashed, horizontal line in panels (*a*)–(*c*) corresponds to the reversal surface, where $B_\phi = 0$.

toroidal component of the flow [15, 16], measured in RFX by means of the gas-puff imaging (GPI) technique [25, 26]. The GPI shows that the flow reverses direction toroidally, with the development of two null points (source and stagnation points), as shown in figure 2(*a*) (arrows and the solid, blue line). To understand the presence of these two null points, we observe that the edge magnetic topology of the MH state is dominated by the ($m = 0, n = 1$) mode (wavelength=the entire toroidal circumference), and the superposition of the $m = 1$, $n = 7$–23 modes. The $m = 0$ modes resonate at the reversal surface $q = 0$, where $B_\phi = 0$, and form a chain of islands [12, 13] with multiple n's, with $n = 1$ the largest in the MH state. Figure 2(*a*) shows, together with the flow, a Poincaré plot where, for simplicity, only the (0, 1) mode is plotted: the reversal surface is marked as a horizontal, dashed line. The main source of particles is independent of the $m = 0$ modes, being aligned with the maximum $m = 1$ bulge at $\phi = \phi_{\rm lock}$ ('locking angle', figure 2(*d*)), where the plasma-wall interaction (PWI) is also maximum[2], a well-known result in the RFP [27]. In contrast, the stagnation point for the plasma flow corresponds to the X-point of the (0, 1) island and to the maximum radiation, at $\phi - \phi_{\rm lock} \sim 100^\circ$ (figure 2(*b*)). The toroidal convective flux associated with the flow reversal can be easily calculated as $v_\phi n_{\rm edge} = 15\,{\rm km\,s^{-1}} \cdot 10^{19}\,{\rm m^{-3}} \simeq 10^{23}\,{\rm m^{-2}\,s^{-1}}$, which exceeds the local radial diffusive flux by more than one order of magnitude [14]: it is this huge convective flux that causes the edge density peaking, which is clearly visible in figure 2(*c*) in the same toroidal region of the maximum radiation, with a local density exceeding 10^{20} m $^{-3}$. This is sufficient to conclude that the particle accumulation is due to the flow reversal, in the form of a huge convective cell that carries matter from the maximum $m = 1$ bulge at $\phi - \phi_{\rm lock} = 0$, right to the X-point of the (0, 1) island at $\phi - \phi_{\rm lock} \sim 100^\circ$, and that a crucial role for reversing the flow is evidently played by the X-point of the (0, 1) island. The particle confinement is therefore determined by the flows and related electric fields in the edge, as shown by the density map in figure 2(*c*). In this view, the dependence of this phenomenology on the empirical threshold $n_{\rm e} \approx n_{\rm G}$, more than defining a parameter space for RFP operation, indicates a dependence of particle confinement on the ratio $n_{\rm e}/I_{\rm p}$, which can be translated into a collision frequency: in fact, $n_{\rm e}/n_{\rm G} \propto \nu\tau_{\rm tor}$, collision frequency normalized to a particle toroidal transit time, $\tau_{\rm tor} = 2\pi R_0/v_{\rm th}$, with $v_{\rm th}$ thermal velocity. This fact relates the RFP high-density flows and particle accumulation to RMP experiments in tokamaks, where particle confinement depends on the edge magnetic topology [20].

3. Test particle simulations

3.1. The code and connection lengths

To simulate the flow pattern presented so far, we make use of the guiding-centre code Orbit [19] to analyse the magnetic field topology and the motion of monoenergetic electrons and ions embedded in the magnetic field, initially without potential. Boozer coordinates are used in Orbit, $\psi_{\rm p}, \theta, \zeta$ ($\psi_{\rm p}$ poloidal flux and $\zeta = \phi - \nu(\psi_{\rm p}, \theta)$, ν function necessary to get the Jacobian proportional to the field, $\mathcal{J} \sim 1/B^2$). A great advantage in the RFP configuration is that the perturbations are known with fairly good accuracy: the radial profile ('eigenfunction') of the $m = 0, 1$ and $n = 1 - 23$ global, kink-tearing modes can be calculated through a linearization of the finite-conductivity, MHD equations. This was shown by Robinson in 1978 [28], which is essentially the analogue of Newcomb's analysis [29] for a diffuse pinch. In RFX-mod we use the refinement of this theory, brought about by Fitzpatrick, Zanca and Terranova in toroidal geometry, with the experimental pick-up coil spectra used as constraints [30, 31]. Generally speaking, Orbit can accept any radial function

[2] Usually in MH studies the toroidal location of the $m = 1$ bulge, $\phi_{\rm lock}$, is the zero for comparing different measurements along the toroidal angle. In the remainder of the paper all toroidal angles will be normalized to $\phi_{\rm lock}$, or $\zeta_{\rm lock}$ in Boozer coordinates.

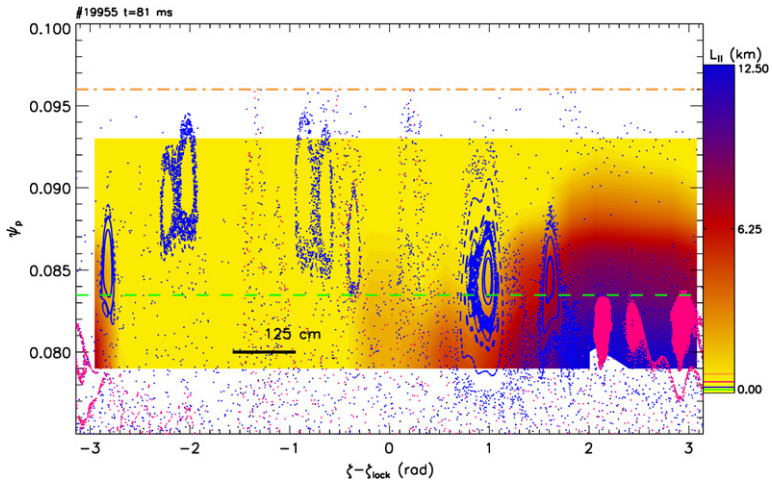

Figure 3. Poincaré plot as obtained from the ORBIT code, equatorial cut at $\theta = 0$. Color codes indicate the electron characteristic length $L_\parallel$ defined as the length of the path followed by the electrons parallel to the magnetic field from their initial position $(\psi_{p,1}, \theta_1, \zeta_1) = (0.093, \text{random}, \zeta_1)$ to their exit position $(\psi_{p,2}, \theta_2, \zeta_2) = (\psi_{p,2}, \text{random}, \text{random})$. The map describes $L_\parallel(\zeta_1, \psi_{p,2})$, each point $(\zeta_i, \psi_{p,j})$ of the grid being the initial toroidal angle and final radius of a single run, $\zeta_i = \zeta_1$ and $\psi_{p,j} = \psi_{p,2}$. The dashed, horizontal line corresponds to the reversal surface, the dashed-dotted line to the wall, $\psi_p = \psi_w$.

as input perturbation: in the RFP we have also used those calculated from a non-linear, visco-resistive MHD code [2, 12]. The sole approximation is that in the code enters the scalar function $\alpha(\psi_p)$, obtained through the relation $\delta\boldsymbol{B} = \nabla \times \alpha \boldsymbol{B}_o$, $\boldsymbol{B}_o$ being the equilibrium magnetic field. With this position, the Hamiltonian (toroidal flux in the RFP choice [32]) $H = \psi$ for the field lines becomes the sum of two terms

$$H(\psi_p, \zeta; \theta) = \int q \, d\psi_p + \sum_{m,n=1}^{23} \left(\frac{m}{n} g + I\right) \alpha_{m,n}(\psi_p) \times \sin(m\theta - n\zeta + \phi_{m,n}), \quad (1)$$

g, I being the covariant components of the field in ORBIT notation [19], $\phi_{m,n}$ the experimental phases of the modes. The associated canonical equations are

$$\frac{d\psi_p}{d\theta} = -\frac{\partial H}{\partial \zeta}, \quad (2)$$

$$\frac{d\zeta}{d\theta} = \frac{\partial H}{\partial \psi_p} = q(\psi_p). \quad (3)$$

In this way, for each $m = 0, n$ component, $\alpha_{0,n}$ becomes the usual Hamiltonian 'perturbation' parameter, and the Hamiltonian has the form

$$H(\psi_p, \zeta) = H_0(\psi_p) + \alpha H_1(\psi_p, \zeta), \quad (4)$$

which is independent of the 'time' θ, which justifies the presence of conserved $m = 0$ islands at the reversal surface, $q = 0$ [12, 13]. Collisions enter through a pitch-angle scattering operator, implemented by taking into account ion–ion, ion-electron, electron–electron, electron–ion and ion-impurity encounters, using the Kuo–Boozer approach [33]. The pitch-angle scattering operator thus describes the exchange of momentum between particles, due to a Coulomb scattering: in the code it is implemented as a diffusion operator in the space of the 'pitch' parameter, $\lambda = v_\parallel/v$. It is therefore the ordinary way particles can be trapped and de-trapped in a magnetic mirror [34]. Finally, since the standard ORBIT boundary is perfectly absorbing ($R = 0$), which is suited for simulating fast-particle losses [35], we had to modify it [16] to account for recycling $R = 1$, in order to deal with the RFX-mod first wall, which is fully covered by graphite tiles [36]. In our scheme, if a particle hits the wall, it is lost and replaced by a new particle, at a distance of one ion gyroradius ρ_i from the wall, the same (θ, ζ), but with a new random pitch.

To characterize the RFX-mod edge, let us analyse first the connection length of the topology shown in figure 2(*a*). Define a grid in radius and toroidal angle, $(\zeta_i, \psi_{p,j})$. Let us consider electrons (ions have larger gyroradii, ∼1 cm in the RFX edge, so they average out the field in one gyroradius), and define the parallel connection length as $L_\parallel(\psi_p, \theta, \zeta) \simeq v_{th}\tau_{trav}$, τ_{trav} being the electron travel time between the initial $(\psi_{p,1}, \theta_1, \zeta_1)$ and final positions $(\psi_{p,2}, \theta_2, \zeta_2)$. Assign one point of the grid to the initial toroidal angle, $\zeta_1 = \zeta_i$, and the other one to the recovery radius, $\psi_{p,2} = \psi_{p,j}$: in this way each point in the grid corresponds to an individual run. The initial radius is fixed for all runs, $\psi_{p,1} = 0.093$, and corresponds to $r \simeq 44.6$ cm, $r/a = 0.97$, which is ∼$2\rho_i$ ion Larmor radii from the wall, $\psi_w = 0.096 \equiv a = 45.9$ cm (a Larmor ion radius for the parameters of this run is $\rho_i \sim 8$ mm, 2×10^{-3} in ψ_p units). The initial poloidal angle is random, and we disregard the final poloidal and toroidal angles: in this way, initial and final conditions are $(0.093, \text{random}, \zeta_i)$ and $(\psi_{p,j}, \text{random}, \text{random})$, $1 \leqslant i \leqslant 25$ and $1 \leqslant j \leqslant 15$. For each run we launch 1000 electrons, and follow them for 1000 toroidal turns until the stop condition $\psi_p = \psi_{p,j}$ is reached for at least 500 particles (half loss stop), with energy 260 eV and normalized collision frequency $\nu_e\tau_{tor} = 1.42$. At the end of the run we register $L_\parallel$, which represents the path electrons follow along the field lines from $2\rho_i$ Larmor radii next to the wall, to the recycling wall and back to $\psi_{p,j}$, for a fixed toroidal slice ζ_i. Figure 3 shows a contour map of $L_\parallel(\zeta_i, \psi_{p,j})$, overplotted to the Poincaré section of the edge, for a RFX-mod discharge near the Greenwald limit (discharge # 19955, time 81 ms, $n_e/n_G = 0.8$). The Poincaré section is performed by

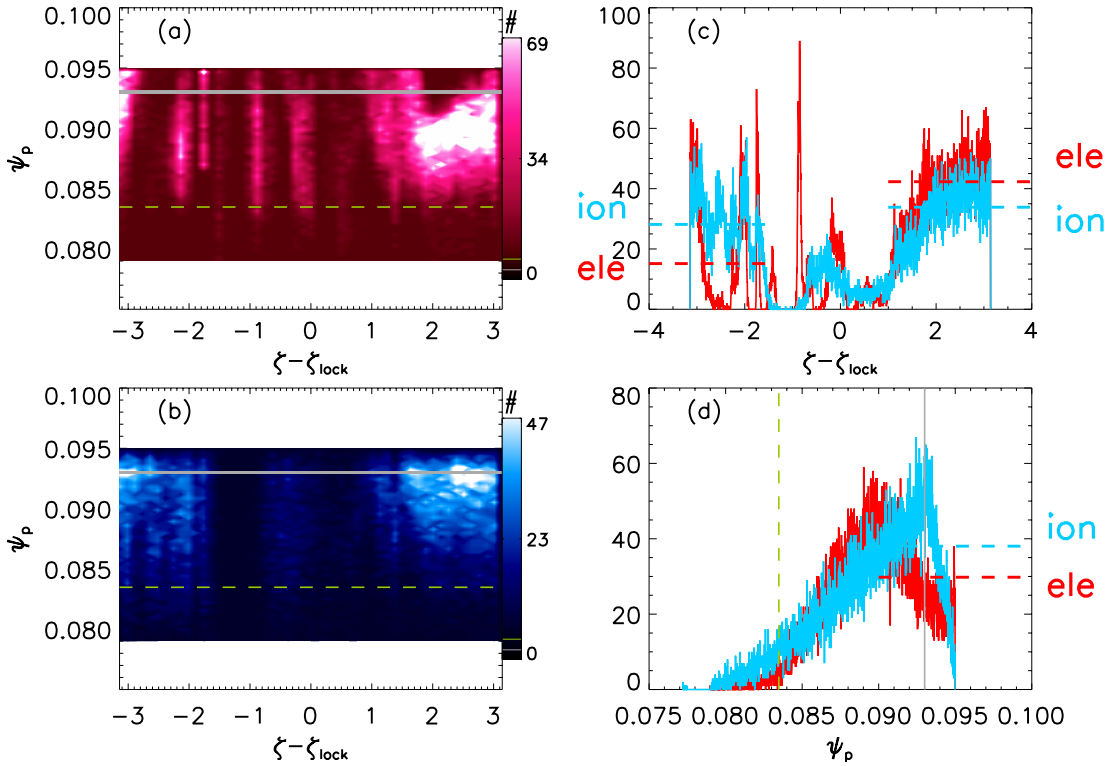

Figure 4. Diffusion plots of electrons and ions: (*a*) 2D pdfs $N(\zeta, \psi_p)$ of final positions taken by electrons at the end of the run, colour code indicates number of particles in each (ζ, ψ_p) bin; (*b*) the same for ions; (*c*) pdf of angles N_ζ (red=electrons, blue=ions); (*d*) pdf of radii N_{ψ_p}.

adding all the $m = 0, 1, n = 1-23$ modes in the spectrum: the topology is much more complicated now than in figure 2(*a*). Two effects combine: higher $m = 0$ harmonics determine a multiplicity of islands which correspond to the secondary maxima of the 'potential'

$$H_1 = \sum_{n=1}^{23} I\alpha_{0,n}(\psi_p)\sin(-n\zeta + \phi_{m,n}) \ . \qquad (5)$$

The second effect is that the addition of the $m = 1$ modes determines the creeping of chaos in the separatrices of the $m = 0$ islands [12]. Despite these complications, the map of $L_\parallel$ shows a clear $n = 1$ modulation along the toroidal angle ζ, being $L_\parallel \sim 12$ km near the X-point of the (0, 1) island, and $L_\parallel \sim 50$ m near the O-point, two orders of magnitude difference (compare the map of $L_\parallel$ in figure 3 with the simplified Poincaré map of figure 2(*a*)). This is the confirmation of the theoretical result that X-points possess *structural stability*, namely, a perturbed X-point remains an X-point [37]. The mechanism acting in the edge of the MH RFP near the (0, 1) X-point is therefore similar to the homoclinic manifolds operating in the vicinity of the X-point of a tokamak divertor [7, 38], and this similarity can be extended also in the helical state of RFX-mod, as shown in [39]. In contrast, the behaviour near the (0, 1) O-point is a free streaming of electrons along chaotic field lines that intercept the wall, which can be paralleled by the 'density pump-out' phenomenon in tokamak plasmas with RMPs [40]. Of course, the picture of electrons free-streaming to the wall is naive, since immediately a strong ambipolar potential builds up to balance radial diffusion. But this will happen at the expense of the symmetry in the toroidal angle. In fact, given so a large difference in the radial diffusion of electrons along the toroidal angle, one can expect the ambipolar potential to possess a $m = 0, n = 1$ symmetry, parent to the symmetry of the island that generates differential radial electron diffusion.

3.2. Diffusion plots

The connection length behaviour shown in section 3.1 for electrons is expected to generate a differential electron-to-ion diffusion rate, modulated along ζ. To demonstrate this, let us consider diffusion plots of electrons and ions, for the same topology of figure 3. Initiate a wide distribution of a large number (6×10^4) of electrons and H^+ ions deposited at $\psi_p(0) = 0.093$ ($r \simeq 44.6$ cm, $r/a = 0.97$, the same as in the run of section 3.1), and θ, ζ random. Particles are monoenergetic, with the same energy $T_e = T_i = 260$ eV. Collect particles at $\psi_p = 0.079$ ($r \simeq 39$ cm, $r/a = 0.85$), and stop the run when half of the particles cross the collection surface: then analyse the distribution of final positions taken by particles remaining in the domain, between $\psi_p = 0.079$ and the wall $\psi_w = 0.096$. The choice of stopping the run with a half-loss condition is somewhat arbitrary, but it allows for evolving the system to an equilibrium between conserved and lost particles, with good statistics to define the outward fluxes [41]. According to the dominant geometry, we will discard the θ angle, and consider the 2D-probability distribution function (pdf) $N(\zeta, \psi_p)$ of toroidal angle and radius. Results are shown in figure 4: panel (*a*) shows the bi-dimensional distribution of electrons, where the colour code represents the number of particles in each (ζ, ψ_p) bin, and the horizontal, grey solid

line at $\psi_p = 0.093$ marks the deposition surface. The reversal surface is marked by the horizontal green-dashed line. Overall, electrons tend to accumulate at $\zeta - \zeta_{lock} = 2$–3 radians, namely, the region of long connection lengths of figure 3, as expected. The region of the O-point of the (0, 1) island is devoid of electrons, but with radially and toroidally localized 'holes', corresponding to the secondary $m = 0$ islands (secondary maxima of H_1 in equation (5)). These holes are generated by motion on a very short timescale (compared with the run time), and they could correspond to Lévy flights [42–44], which on the other hand have been identified up to now only in the core of the chaotic state of the RFP [2]. In contrast, electrons tend to accumulate around the secondary X-points (secondary minima of H_1), where connections lengths are larger. Simply stated, electrons follow closely the magnetic topology. Let us consider now ions: figure 4(*b*) shows the bi-dimensional distribution of ions at the end of the run. The distribution is more uniform, both in the angle ζ and radius ψ_p: radially, most ions diffuse only a few Larmor radii from the deposition surface (horizontal, grey solid line), which is reasonable since the magnetic topology in the RFP edge shows a degree of order sufficient to slow down ion transport considerably from the chaotic, MH level typical of the core plasma, to a level closer to the neoclassical baseline [12]. Toroidally, ions average out details of the magnetic topology which are of the order of their Larmor radius, and their drifts are also larger. These two effects combine to produce a more uniform diffusion in the magnetic field along the toroidal angle: there is only a local 'hole' of ions around the locking angle at $\zeta = \zeta_{lock}$, corresponding to the maximum $m = 1$ bulge, which is a well-known region of increased PWI [27], as shown previously when discussing figure 2(*d*).

To compare directly electron and ion distributions, in figure 4(*c*) we compute the angular pdfs, by integrating N along the radial coordinate, $N_\zeta = \int d\psi_p N(\zeta, \psi_p)$, and plot them together: apart from the region around $\zeta - \zeta_{lock} = 0$, where the statistics for both electrons and ions is rather poor, there is a local excess of electrons at $\zeta - \zeta_{lock} \sim 2$ radians (X-point of the (0, 1) island) and a local excess of ions (with respect to electrons) at $\zeta - \zeta_{lock} \sim -2$ rad (O-point of the (0, 1) island). The two horizontal, dashed lines correspond to the average value of the distributions N_ζ in the regions left and right to ζ_{lock}, and help us to visualize the differences in ion and electron motion in those regions: this makes evident that ion distributions are uniform left and right to ζ_{lock}, while electrons are strongly asymmetric. Electrons are therefore responsible for the charge imbalance, through the mechanism of the homoclinic manifolds (acting mainly on electrons!) discussed in section 3.1. In this way, we can expect *the ambipolar potential to possess the same symmetry of the parent island*.

It is worth noting that the charge imbalance near the X-point of the (0, 1) island shown on the right of ζ_{lock} in figure 4(*c*) is *not directly* the density accumulation in the MARFE-like structure shown in figure 2. In fact, a simple argument based on the experimental values of E_r in the edge gives a local excess of electrons $\rho_e \lesssim 10^{14} m^{-3}$ near the X-point, to be compared with the edge density peak $n_e \approx 10^{20} m^{-3}$ [16]. The charge imbalance generates the electrostatic potential Φ, and Φ generates the flow which is ultimately responsible for the MARFE.

Finally, let us comment the radial distribution, integrated along the angle, $N_{\psi_p} = \int d\zeta N(\zeta, \psi_p)$, shown in figure 4(*d*): the deposition radius corresponds to the vertical, solid grey line, the reversal is the green-dashed line. The behaviour of N_{ψ_p} shows that, if one averages out the toroidal asymmetries, there is a local cloud of positive charge next to the wall, which extends $\sim 3\rho_i$ ion Larmor radii from the wall (recall here that $\rho_i = 2 \times 10^{-3}$ in ψ_p units). This is a combined effect of recycling $R = 1$ and larger electron mobility (of Lévy-type [2], or not): the final outcome is an electric field whose radial component is (on average over the toroidal angle) inward-pointing, as seen in measurements on RFX [45, 46]. The picture we get here is anyway more complicated than a finite-Larmor radius effect [47], and could be a caveat for the tokamak experiments of RMP: when inducing chaos in the edge, a differential electron-to-ion motion (nearly ballistic for electrons, nearly neoclassical for ions) builds up almost immediately a potential, whose direction depends on the wall conditions, and whose symmetry is parent to the islands generated in the edge. In fact, the electric field dependence on the angular coordinate θ has already been simulated in the tokamak [48].

4. The ambipolar potential

4.1. The model for the potential

The problem of a self-consistent evaluation of an electric field within ORBIT (using Poisson's equation to determine step by step the potential needed for ambipolarity) requires following together electron and ion dynamics, i.e. matching temporal steps which are a factor $\sqrt{m_i/m_e}$ different: this is an extension to a whole different world, similar to the gyrokinetic simulations. A self-consistent calculation of the potential can be done within simplified dynamics, i.e. maps, such as the 'twist map' [49], and has been successfully applied to tokamaks by Spatschek and collaborators [11, 38, 50]. Here we will follow a much simpler approach, already followed in the RFP helical state [41, 51]: we maintain the separation between electron and ion runs, and impose an analytic function for the potential $\Phi(\psi_p, \theta, \zeta)$ which can be inserted in the guiding-centre equations of motion. To build the function Φ one can obviously use the results of section 3.2, but much more valuable is the knowledge of experimental data to compare with. The criteria are:

(i) $\partial\Phi/\partial\theta = 0$;
(ii) the angular dependence in ζ has to balance electron and ion distributions, so it has to speed up electrons in the X-point of the (0, 1) island, and trap them near the O-point;
(iii) the radial profile (radial potential well) should be guessed from existing data, namely those described in [45, 46];
(iv) it has to retain the main features of figure 4, without caring too much about the details of secondary islands.

The simplest analytical form for the potential reads:

$$\Phi(\psi_p, \zeta) = -E_a \psi_p - \frac{1}{2} E_{r,w} \left[\sigma_{\psi_p} \log\left(\cosh\left(\frac{\psi_p - \psi_{p,rv}}{\sigma_{\psi_p}} \right) \right) + \psi_p \right] \times \left(2e^{-(\zeta-\zeta_0)^2/2\sigma_\zeta^2} - 1 \right), \quad (6)$$

Table 1. Guess values for the parameters describing the ambipolar potential.

Parameter	Value
$E_{r,w}$	$3.5\,\mathrm{kV\,m^{-1}}$
ζ_0	1.74 rad (=100°)
σ_ζ	0.87 rad (=50°)
$\psi_{\mathrm{p},rv}$	0.083
σ_{ψ_p}	$5\times10^{-3}=2.5\rho_\mathrm{i}$
E_a	$-1.5\,\mathrm{kV\,m^{-1}}$

where for simplicity now ζ is taken as already normalized to ζ_{lock}. There are six free parameters, whose initial values are reported in table 1: the radial position and width of the potential well, $\psi_{\mathrm{p},rv}$ and σ_{ψ_p}, the toroidal position and width of the potential well, ζ_0 ('potential phase') and σ_ζ, the negative baseline of the radial electric field, E_a, and the potential amplitude, $E_{r,\mathrm{w}}$.

The initial guess for the potential amplitude and phase are $E_{r,w}=3.5\,\mathrm{kV\,m^{-1}}$ and $\zeta_0\sim\pi/2=\zeta_X$: the amplitude matches old RFX measurements [46], the phase makes the potential well coincide toroidally with the location of the X-point of the (0, 1) island. The guess for the phase is somewhat justified by the need of speeding up electrons sticking around the X-point, and trap those free-streaming to the wall near the O-point. Differentiate equation (6)

$$E^{\psi_\mathrm{p}}(\psi_\mathrm{p},\zeta)=-\frac{\partial\Phi}{\partial\psi_\mathrm{p}}=E_\mathrm{a}+\frac{1}{2}E_{r,w}\left[\tanh\left(\frac{\psi_\mathrm{p}-\psi_{\mathrm{p},rv}}{\sigma_{\psi_\mathrm{p}}}\right)+1\right]\times\left(2\mathrm{e}^{-(\zeta-\zeta_0)^2/2\sigma_\zeta^2}-1\right). \quad (7)$$

Equation (7) takes the form of figure 5(*a*), dash-triple dot line: in the potential well $\zeta=\zeta_0$ the radial electric field in the edge is positive, and changes sign at $\psi_\mathrm{p}=\psi_{\mathrm{p},rv}-\sigma_{\psi_\mathrm{p}}=0.077$, which corresponds to ∼38 cm ($r/a=0.83$). The inflection point $\psi_\mathrm{p}=\psi_{\mathrm{p},rv}$ corresponds to the potential well, and is guessed to be the reversal radius, according to our initial hypothesis that the ambipolar field is generated by the (0, 1) island resonating at $q=0$. For $\zeta\neq\zeta_0$, E^{ψ_p} becomes negative, with the most negative value acquired at $\zeta=-\pi/2$, namely, at π distance from ζ_0, right into the potential hill. The behaviour of the radial electric fields mimics old RFX data showing the edge E_r changing sign along ϕ, coherently with v_ϕ [46]. The guess for the radial half-width of the potential well, $\sigma_{\psi_\mathrm{p}}=5\times10^{-3}$ equivalent to $2.5\rho_\mathrm{i}$ ion Larmor radii, is consistent with the results of section 3.2, and with measurements in the old RFX [45]. The bias $E_\mathrm{a}<0$ is guessed to match the values of $E_r(a)$ given in [46]; in the core, the model (equation (7)) assumes the electric field levelling off to E_a, since our simulations never explore the plasma $\psi_\mathrm{p}<0.079$.

The angular dependence of the potential (equation (6)) is derived from recent data from the GPI diagnostic [25, 26], which have been briefly recalled in section 2. In particular, as a first guess we choose $\zeta_0\sim\pi/2=\zeta_X$ and $\sigma_\zeta=50°$, which corresponds to choosing a potential well centred in the (0, 1) X-point, 100° toroidal degrees wide: the final contour plot of $\Phi(\psi_\mathrm{p},\zeta)$ is shown in figure 5(*b*). The most noteworthy feature of our potential model is the presence of a saddle point at $\zeta=\zeta_0$: along the radius the potential shows a peak at $\psi_\mathrm{p}=\psi_{\mathrm{p},rv}$, while along the angle it has a minimum at $\zeta=\zeta_0$. Insert these values in equation (6) to obtain the potential at the saddle point

$$\Phi(\psi_{\mathrm{p},rv},\zeta_0)=-(E_\mathrm{a}+\tfrac{1}{2}E_{r,w})\,\psi_{\mathrm{p},rv}\,, \quad (8)$$

shown clearly as an X-shaped contour in figure 5(*b*). The region of the saddle point (inset in figure 5(*b*)) is crucial from the point of view of transport: generally speaking, as a consequence of $(\partial\Phi)/(\partial\zeta)\neq0$, a toroidal component of the electric field appears, one order of magnitude smaller than the radial one (minimum $E^\zeta=-0.25\,\mathrm{kV\,m^{-1}}$, minimum $E^{\psi_\mathrm{p}}=-5\,\mathrm{kV\,m^{-1}}$). Around the saddle point, this brings about the formation of a convective cell, shown as an expanded inset in figure 5(*c*). The particle motion in presence of the saddle point complicates the simple picture of particle diffusion in the magnetic field: it appears as a periodic component (oscillation) down the potential, plus an $\boldsymbol{E}\times\boldsymbol{B}$ drift across the potential, which can be seen along with many oscillations up and down Φ as a convective term $\boldsymbol{v}\cdot\nabla\Phi=0$ on the equipotential surfaces that conserves kinetic energy. This convective term along the equipotential surfaces is likely to coincide with the GPI flow that determines particle confinement in the RFP edge, as described in section 2.

Finally, it is worth underlining that Φ is not a flux function, $\Phi\neq\Phi(\psi)$ with ψ defined by equation (1), which is the usual choice when considering the ambipolar field generated by an island [41, 51]. This latter choice is justified by the fact that electrons average out any charge imbalance along ψ, provided ψ does not intercept the first wall. But this is not our case (see e.g. figure 3), thus our equipotential surfaces are not flux surfaces, $\boldsymbol{v}\cdot\nabla\psi\neq0$ and the convective term will cause effective transport across the magnetic field. The flux surfaces ψ overlapping the first wall is therefore a necessary condition for generating convective cells and MARFE phenomena, as found experimentally both in the RFP [16, 52] and the tokamak [53].

4.2. *Particle transport with the potential*

Here we want to apply the analytic form of the potential to Orbit runs. Of the six free parameters, four can be fixed to their guess values of table 1 without losing generality. Those are $\psi_{\mathrm{p},rv}$, which can be fixed to the reversal radius on the basis both of theory (section 3) and experiment [46]; the bias E_a, which is independent of the (0, 1) modulation; and finally the radial and toroidal widths σ_{ψ_p} and σ_ζ, which change only the details of electron and ion orbits without adding much to the basic physics of the ambipolar potential. There remain only two parameters left, which are fundamental in determining the potential behaviour: the potential amplitude $E_{r,w}$ and phase ζ_0.

The amplitude can be easily determined in simulations by varying the free parameter $E_{r,w}$ until electrons of a given energy are trapped toroidally in the potential: this is a simple, necessary condition for the ambipolar field to work properly. Launch many single particle runs corresponding to electrons of different energies, no collisions and no perturbations, $\zeta_0=100°$ as in table 1, start from the guess value $E_{r,w}=3.5\,\mathrm{kV\,m^{-1}}$ and vary it until a closed orbit in ζ is reached around ζ_0.

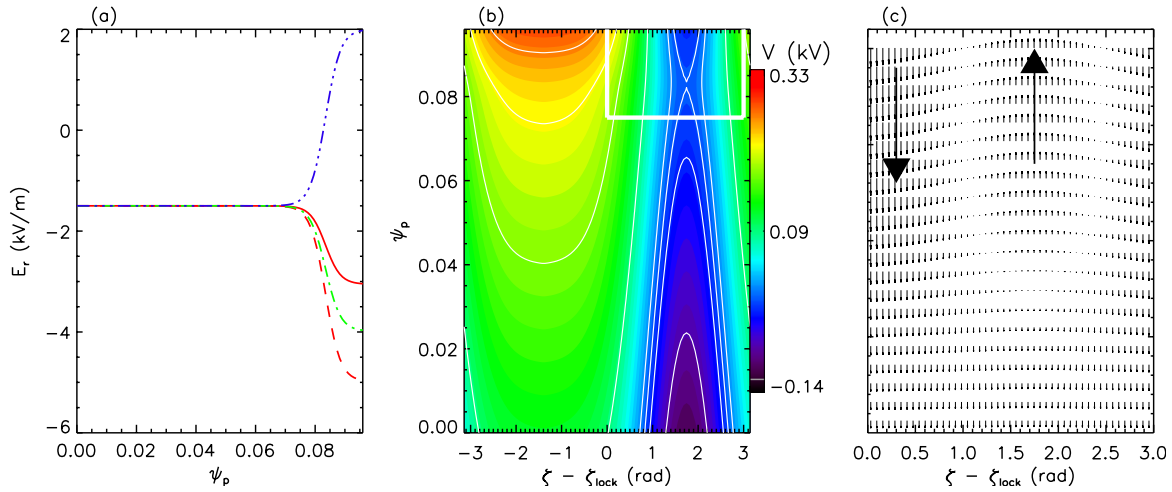

Figure 5. Analytical model for the ambipolar potential, parameters are initial guesses as in table 1: (*a*) radial dependence of $E^{\psi_p} = -(\partial\Phi/\partial\psi_p)$ ('radial' electric field) at different angles: solid line, $\zeta = -\pi$, dashed line − − −, $\zeta = -\pi/2$, dashed-dotted −. − .−, $\zeta = 0$, dash triple dot −... − ...−, $\zeta = \pi/2$. (*b*) Contour plot of the potential $\Phi(\zeta, \psi_p)$: the saddle point corresponds to $\zeta_0 = 100^\circ$ and $\psi_p = \psi_{p,rv} = 0.083$. (*c*) For the inset in (*b*), the vector field describing the electric field E^{ψ_p}, E^{ζ}, showing the development of a convective cell in correspondence to the saddle point depicted in panel (*b*).

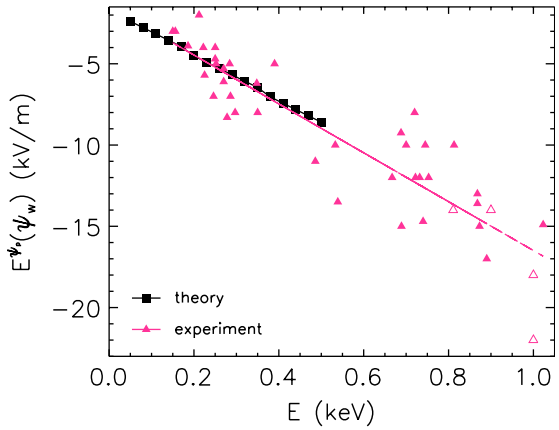

Figure 6. Radial electric field at the wall $E^{\psi_p}(\psi_w) = E_a - E_{r,w}$ as a function of electron energy, in the code (black, full squares ■), and corresponding measurement E_r(a) in the experiment RFX-mod (pink, full triangles ▲). Open triangles (△) correspond to lithized discharges via Lithium pellets.

Choosing ζ_0 as in table 1 does not influence the result, since we do not consider perturbations, there is symmetry in ζ and any ζ_0 is equivalent. We compute for each run the radial electric field at the wall, $E^{\psi_p}(\psi_w) = E_a - E_{r,w}$ (equation (7) with $\zeta = \zeta_0 - \pi$ and $\psi_p = \psi_w$). The dependence of $E^{\psi_p}(\psi_w)$ on the electron temperature (energy) is shown in figure 6 (black, full squares ■), with the expected linear dependence on energy, $E^{\psi_p}(\psi_w) = -T_e/eL_{well}$. The proportionality constant is a length, $L_{well} \sim 6.6$ cm, which obviously is in good agreement with the radial extent of the potential well, $L_{well} = 2\sigma_{\psi_p}$. The experimental evaluation of the radial electric field at the edge $E_r(a)$, which corresponds to $E^{\psi_p}(\psi_w)$ in simulations[3], can be done for comparison by means of the GPI. Subtracting from measurements the (expected) contribution of the diamagnetic flow, which in RFX-mod accounts for an average 15% on the total measured flow only, one obtains

$$E_r(a) = \frac{T_i}{Ze}\frac{\nabla P_i}{P_i} + v_\phi B_\theta - v_\theta B_\phi = 0.15E_r + v_\phi B_\theta + \mathcal{O}(B_\phi) \approx 0.15E_r + v_\phi B_\theta\,, \quad (9)$$

given B_ϕ is negligible in the RFP edge compared with B_θ. The measurements are shown in figure 6 as pink, full triangles ▲ over-plotted to simulated values: the agreement between theory and experiment is rather good, showing that the radial electric field measured in RFX-mod is mostly ambipolar, within a 15% uncertainty due to the diamagnetic contribution. The plot shows also a consistency of the chosen radial extent of the potential well.

Finally, let us use the potential to balance electron and ion diffusion with perturbations. Let us repeat the exercise of section 3.2, and launch 6×10^4 electrons and ions in the domain $(0.079 < \psi_p < \psi_w, \theta, \zeta)$ subject to magnetic field, collisions and the potential as in equation (6), other parameters as in table 1. The amplitude has been chosen as $E_{r,w} = 4$ kV/m, according to $E = 260$ eV and figure 6. Define the outward flux

$$\Gamma = \frac{\#\text{particles}}{S \times \text{runtime}}\,, \quad (10)$$

number of particles exiting the domain, divided by the runtime and the bounding surface S at $\psi_p = 0.079$. Each run is performed by varying the only free parameter left, the potential phase ζ_0, which corresponds to the saddle point shown in figure 5(*b*): then look at the fluxes Γ_e and Γ_i. The results are shown in figure 7, where each point represents one single run: on the x-axis we plot the phase difference between the potential saddle point and the X-point of the (0, 1) island, $\Delta\zeta = \zeta_0 - \zeta_X$. We see that we get ambipolarity in ORBIT, within the hypotheses of the code, for $\Delta\zeta = \frac{3}{4}\pi$, which is shifted toroidally of $\sim \pi$ with respect to our initial guess $\Delta\zeta = 0$, or $\zeta_0 = \zeta_X$. This means that the potential causes a toroidal drift of particles and has to readjust the phase from the initial guess $\Delta\zeta = 0$ to

[3] Strictly speaking, the contravariant component of the electric field E^{ψ_p} is not directly comparable to the radial electric field measured in the local triad, $E^{\hat{r}}$. In RFX-mod anyway $E^{\hat{r}} = E^r = -(\partial\psi_p/\partial r)(\partial\Phi/\partial\psi_p) = (\partial\psi_p/\partial r)E^{\psi_p}$. Therefore $E^{\hat{r}} = R_0 B^{\hat{\theta}} E^{\psi_p}$, and since $R_0 = 2$ m and the local $B^{\hat{\theta}}(a) = 0.5$ T finally $E_r(a) \approx E^{\psi_p}(\psi_w)$.

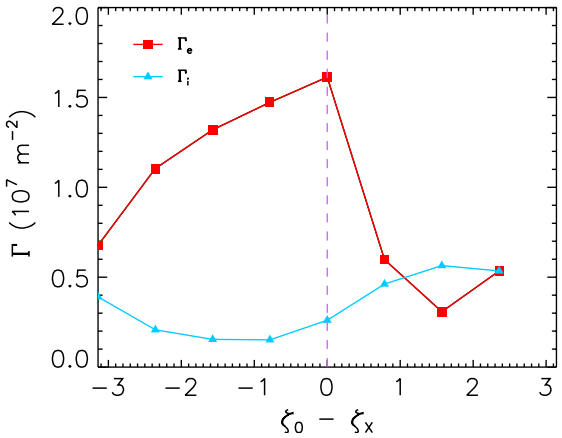

Figure 7. Electron and ion fluxes, Γ_e (red) and Γ_i (blue) as a function of the phase of the potential, relative to the (0, 1) X-point, $\Delta\zeta = \zeta_0 - \zeta_X$. The initial guess $\zeta_0 = \zeta_X$ is marked as a dashed, vertical line: ambipolarity is reached in the code for $\Delta\zeta \approx 3/4\pi$.

match the new particle positions. This is a consequence of the fact that the drifts are not tangent to the toroidal flux surfaces, $\boldsymbol{v} \cdot \nabla\psi \neq 0$. Anyway, the presence of a phase shift $\Delta\zeta \neq 0$ is somewhat justified by the experiment, where $\Delta\zeta \simeq -\pi/2$, namely, the distance between the two vertical, dashed lines in figure 2. This is a necessary condition in experiment to generate a edge density peak (which in the Greenwald limit phenomenology causes the MARFE appearance). In fact, only in that case the main particle source (which depends on the magnetic island) corresponds to the inward-pointing part of the convective cell (which depends on the 'potential' island). We speculate that adding energy-exchanging collisions in Orbit could drastically change the motion in the potential, and the value of $\Delta\zeta$ required for ambipolarity, since they will allow for trapping and de-trapping of particles in the potential well. Our result $\Delta\zeta = \frac{3}{4}\pi$ should therefore be taken as the collisionless limit of our theory. The collision frequency is likely to change the value of $\Delta\zeta$, and switch on the mechanism of convective flux that determines the Greenwald limit in the RFP.

5. Conclusion

In this paper we have shown that magnetic topology and plasma flow deeply influence edge transport in the RFX-mod RFP, in particular the access to high-density regimes, where edge particle accumulation (toroidally localized and poloidally symmetric) limits the global particle confinement. A central role is played by the electric field determined by the ambipolar constraint. The radial component E_r is measured with different techniques, and is a guess for constructing a model of the potential needed for guaranteeing ambipolarity. Restraining our analysis to high-density discharges, numerical simulations with Orbit show that a proper analytic form of the potential can balance the different radial diffusion of electrons and ions subject to magnetic field and collisions with a background, but this happens at the expense of the toroidal symmetry, since the origin of the differential diffusion lies in the fact that electrons accumulate near X-points of $m = 0$ islands resonating at the $q = 0$ surface. In this way, magnetic islands in the edge interacting with a recycling wall can generate a potential which possesses the same symmetry as the parent islands. In the tokamak, the development of a potential not symmetric in the angle could be a drawback of the application of the RMP. In the RFP, a non-toroidally symmetric potential is associated with a convective cell which causes an abnormal edge density accumulation.

Presently, simulations show that collisions do not enter too much in the mechanism governing the development of these convective cells in the RFP edge, but it is worth recalling that Orbit treats pitch-angle scattering only, i.e. the exchange of *momentum* between particles. The next step is to take into account *energy-exchanging collisions*, allowing for trapping and de-trapping of particles in the potential well. This will also allow for exchanging energy with the wall, that will enter directly in the trapping/de-trapping mechanism.

There are evidences that a mechanism similar to that described here in $m = 0$ symmetry for the Greenwald limit, is at work in the helical state (QSH) of the RFP, with a different, $m = 1$ symmetry: measurements of a helical flow associated with the $m = 1, n = 7$ island have recently been reported [54], together with the observation of a helical modulation of edge electron pressure, floating potential, particle influx and radiation losses [17]. It is reasonable that a helical modification of the ion-to-electron diffusion rate in correspondence to edge magnetic islands could generate a mechanism of critical edge density similar to the RFP $m = 0$ case. Experimentally, the QSH operational space is limited in the attainable density at a relatively low value of n_e/n_G, without detectable QSH for $n_e/n_G \gtrsim 0.4$. Nevertheless, while in the $m = 0$ case it is clear that the final limiting mechanism is a radiative condensation due to a over dense plasma, similar to the MARFE, in the QSH case the connection between potential/flow pattern and phenomenology of QSH disappearance is still under debate. From the point of view of the model, formally the Hamiltonian $H = \psi$ describing $m = 0$ islands (equation (1)) can be transformed into a helical Hamiltonian $\bar{H} = \chi$ substituting $\chi = m\psi_p - n\psi$ and $u = m\theta - n\zeta$ [32, 55], with final form:

$$\bar{H}(\psi_p, u) = m\psi_p - n \times \int q \, \mathrm{d}\psi_p - \sum_{m,n} (mg + nI)\alpha_{m,n}(\psi_p) \sin(u + \phi_{m,n}) \,, \tag{11}$$

and associated canonical equations

$$\frac{\mathrm{d}\psi_p}{\mathrm{d}\theta} = -\frac{\partial \bar{H}}{\partial u}, \tag{12}$$

$$\frac{\mathrm{d}u}{\mathrm{d}\theta} = \frac{\partial \bar{H}}{\partial \psi_p} = m - nq(\psi_p). \tag{13}$$

In the case of only one harmonic, e.g. $m = 1, n = 7$, the Hamiltonian is independent of 'time' θ [5], and the analogy between equations (11) and (1) allows us to expect a modulation of $L_\parallel$ along u, similar to the modulation of $L_\parallel$ along ζ of figure 3, with the development of a edge helical potential with $(\partial\Phi/\partial u) \neq 0$, a saddle point and associated convective cell.

From the experimental point of view, it is worth mentioning that the mode frequency in RFX-mod is limited by the combined action of the feedback system and the resistive shell penetration time to ~25–50 Hz [56]. Since the

characteristic rise time of density is ∼40–60 Hz, the recycling pattern is always parent to the magnetic topology, given that neutrals released from the wall are not averaged over many mode periods. In TEXTOR this behaviour is avoided by increasing the mode frequency of applied perturbations: as a result, the occurrence of the MARFE is reduced [8]. In RFX-mod a program of Lithium wall-conditioning, in order to absorb particles, reduce degassing and decouple wall and modes has been undertaken in 2010 [57].

Acknowledgments

This work was supported by the Euratom Communities under the contract of Association between EURATOM/ENEA. The views and opinions expressed herein do not necessarily reflect those of the European Commission. Figure 1 has been conceived together with Dr Margherita Basso. The authors acknowledge many Hamiltonian interactions with Dr Dominique F. Escande. We thank Dr Giovanni Ciaccio for revising the Hamiltonian for the field lines in the RFP choice.

References

[1] Greenwald M. 2002 *Plasma Phys. Control. Fusion* **44** R27–53
[2] Spizzo G., White R.B., Cappello S. and Marrelli L. 2009 *Plasma Phys. Control. Fusion* **51** 124026
[3] Escande D.F., Paccagnella R., Cappello S., D'Angelo F. and Marchetto C. 2000 *Phys. Rev. Lett.* **85** 3169
[4] Lorenzini R. *et al* and RFX-mod Team and Collaborators 2009 *Nature Phys.* **5** 570–4
[5] Cappello S. *et al* 2011 *Nucl. Fusion* **51** 103012
[6] Evans T.E. *et al* 2006 *Nature Phys.* **2** 419–23
[7] Schmitz O. *et al* the DIII-D and TEXTOR Research Teams 2009 *Phys. Rev. Lett.* **103** 165005
[8] Liang Y. *et al* 2005 *Phys. Rev. Lett.* **94** 105003
[9] Hess W.R., DeMichelis C., Mattioli M., Clairet F., Druetta M., Grosman A., Guirlet R., Hutter T., Lasalle J. and Monier-Garbet P. 1995 *Plasma Phys. Control. Fusion* **37** 951
[10] Xu Y., Weynants R.R., Jachmich S., Van Schoor M., Vergote M., Peleman P., Jakubowski M.W., Mitri M., Reiser D., Unterberg B. and Finken K.H. 2006 *Phys. Rev. Lett.* **97** 165003
[11] Wingen A. and Spatschek K. 2010 *Nucl. Fusion* **50** 034009
[12] Spizzo G., Cappello S., Cravotta A., Escande D.F., Predebon I., Marrelli L., Martin P. and White R.B. 2006 *Phys. Rev. Lett.* **96** 025001
[13] Bonfiglio D., Veranda M., Cappello S., Chacón L. and Spizzo G. 2010 *J. Phys.: Conf. Ser.* **260** 012003
[14] Puiatti M.E. *et al* 2009 *Phys. Plasmas* **16** 012505
[15] Puiatti M.E. *et al* 2009 *Nucl. Fusion* **49** 045012
[16] Spizzo G. *et al* 2010 *Plasma Phys. Control. Fusion* **52** 095011
[17] Scarin P. *et al* and the RFX-mod Team 2011 *Nucl. Fusion* **51** 073002
[18] Ortolani S. and the RFX team 2006 *Plasma Phys. Control. Fusion* **48** B371
[19] White R.B. and Chance M.S. 1984 *Phys. Fluids* **27** 2455–2467
[20] Schmitz O. *et al* 2009 *J. Nucl. Mater.* **390–391** 330–4
[21] Unterberg E., Schmitz O., Evans T., Maingi R., Brooks N., Fenstermacher M., Mordijck S., Moyer R. and Orlov D. 2010 *Nucl. Fusion* **50** 034011
[22] Valisa M. and the RFX Team 2004 *Proc. 20th Int. Conf. on Fusion Energy 2004 (Vilamoura, Portugal 2004)* (Vienna: IAEA) CD–ROM file EX/P4–13 http://www-naweb.iaea.org/napc/physics/fec/fec2004/papers/ex_p4-13.pdf
[23] Valisa M., Frassinetti L., Paccagnella R., Puiatti M.E., Sattin F., Scarin P., Spizzo G., Spolaore M., Vianello N. and the RFX Team *Proc. 21st Int. Conf. on Fusion Energy 2006 (Chengdu, China 2006)* (Vienna: IAEA) CD–ROM file EX/P3–17 http://www-naweb.iaea.org/napc/physics/FEC/FEC2006/papers/ex_p3-17.pdf
[24] Lipschultz B. 1987 *J. Nucl. Mater.* **145** 15–25
[25] Agostini M., Cavazzana R., Scarin P. and Serianni G. 2006 *Rev. Sci. Instrum.* **77** 10E513
[26] Agostini M., Scarin P., Cavazzana R., Sattin F., Serianni G., Spolaore M. and Vianello N. 2009 *Plasma Phys. Control. Fusion* **51** 105003
[27] Zanca P., Terranova D., Valisa M. and Dal Bello S. 2007 *J. Nucl. Mater.* **363–365** 733–7
[28] Robinson D. 1978 *Nucl. Fusion* **18** 939
[29] Newcomb W.A. 1960 *Ann. Phys.* **10** 232–67
[30] Fitzpatrick R. and Zanca P. 2002 *Phys. Plasmas* **9** 2707–24
[31] Zanca P. and Terranova D. 2004 *Plasma Phys. Control. Fusion* **46** 1115
[32] Finn J.M., Nebel R. and Bathke C. 1992 *Phys. Fluids* B **4** 1262–79
[33] Boozer A.H. and Kuo-Petravic G. 1981 *Phys. Fluids* **24** 851–9
[34] White R.B. 2006 *The Theory of Toroidally Confined Plasmas* 2nd edn (London: Imperial College Press) p 75
[35] White R. 2012 *Commun. Nonlinear Sci. Numer. Simul.* **17** 2200–14
[36] Zaccaria P., Dal Bello S. and Marcuzzi D. 2003 *Fusion Eng. Des.* **66–68** 289–93 *22nd Symp. on Fusion Technology*
[37] Lichtenberg A.J. and Lieberman M.A. 1992 *Regular and Chaotic Dynamics* 2nd edn (New York: Springer) p 305
[38] Wingen A., Evans T.E., Lasnier C.J. and Spatschek K.H. 2010 *Phys. Rev. Lett.* **104** 175001
[39] Martines E., Lorenzini R., Momo B., Munaretto S., Innocente P. and Spolaore M. 2010 *Nucl. Fusion* **50** 035014
[40] Evans T. *et al* 2008 *Nucl. Fusion* **48** 024002
[41] Predebon I., Marrelli L., White R.B. and Martin P. 2004 *Phys. Rev. Lett.* **93** 145001
[42] del Castillo-Negrete D. 2008 *Turbulent Transport in Fusion Plasmas* vol 1013, ed S. Benkadda (New York: AIP) pp 207–39
[43] del-Castillo-Negrete D., Mantica P., Naulin V., Rasmussen J. and JET EFDA contributors 2008 *Nucl. Fusion* **48** 075009
[44] Sanchez R., Newman D.E., Leboeuf J.N. and Decyk V.K. 2011 *Plasma Phys. Control. Fusion* **53** 074018
[45] Antoni V., Desideri D., Martines E., Serianni G. and Tramontin L. 1997 *Phys. Rev. Lett.* **79** 4814–17
[46] Puiatti M. *et al* 2001 *J. Nucl. Mater.* **290–293** 696–700
[47] Bartiromo R. 1998 *Phys. Plasmas* **5** 3342–9
[48] Kolesnikov R.A. 2011 *Phys. Plasmas* **18** 014504
[49] Abdullaev S.S., Finken K.H., Kaleck A. and Spatschek K.H. 1998 *Phys. Plasmas* **5** 196–210
[50] Wingen A. and Spatschek K.H. 2008 *Phys. Plasmas* **15** 052305
[51] Gobbin M., Spizzo G., Marrelli L., Terranova D., Martines E., Momo B., White R.B. and Pomphrey N. 2010 *Proc. 37th EPS Conf. on Plasma Physics (Dublin, Ireland, 2010)* vol 34A p P1.1034 http://ocs.ciemat.es/EPS2010PAP/pdf/P1.1034.pdf
[52] De Masi G., Cavazzana R., Fassina A., Martines E., Momo B. and Moresco M. 2011 *Nucl. Fusion* **51** 053016
[53] de Vries P.C., Rapp J., Schüller F.C. and Tokar' M.G. 1998 *Phys. Rev. Lett.* **80** 3519–22

[54] Bonfiglio D., Bonomo F., Piovesan P., Piron L. and Zaniol B. 2010 *Proc. 37th EPS Conf. on Plasma Phys. (Dublin, Ireland, 2010)* vol 34A p O2.101 http://ocs.ciemat.es/EPS2010PAP/pdf/O2.101.pdf

[55] Martines E. *et al* 2011 *Plasma Phys. Control. Fusion* **53** 035015

[56] Zanca P. 2009 *Plasma Phys. Control. Fusion* **51** 015006

[57] Dal Bello S., Innocente P., Agostini M., Alfier A., Auriemma F., Canton A., Carraro L., Cavazzana R., De Masi G. and Mazzitelli G. 2010 *Proc. 23rd IAEA Fusion Energy Conf. (Daejeon, Korea, 2010)* CD-ROM file EXD/P3-06 http://www-pub.iaea.org/MTCD/Meetings/PDFplus/2010/cn180/cn180_papers/exd_p3-06.pdf